

Shale Pore Characterization Using NMR Cryoporometry with Octamethylcyclotetrasiloxane as the Probe Liquid

Qian Zhang,^{†,‡} Yanhui Dong,^{*,†,‡,§} Shimin Liu,[§] Derek Elsworth,[§] and Yixin Zhao^{||}

[†]Key Laboratory of Shale Gas and Geoenvironment, Institute of Geology and Geophysics, Chinese Academy of Sciences, Beijing 100029, China

[‡]University of Chinese Academy of Sciences, Beijing 100049, China

[§]Department of Energy and Mineral Engineering, G3 Center and EMS Energy Institute, The Pennsylvania State University, University Park, PA 16802, United States

^{||}College of Resources & Safety Engineering, China University of Mining and Technology, Beijing 100083, China

ABSTRACT: Fluid flow and chemical transport within shale are determined by the pore size distribution and its connectivity. Because of both low porosity and small (nanometer) pore size, common characterization methods, such as mercury injection capillary pressure (MICP) and the nitrogen adsorption method (NAM), have limited resolution and applicability. Nuclear magnetic resonance cryoporometry (NMR-C) is a novel characterization method that exploits the Gibbs–Thomson effect and provides a complementary method of characterizing aggregate pore structure at fine resolution. We use water and octamethylcyclotetrasiloxane (OMCTS) as probe liquids for NMR-C on controlled porosity samples of SBA, CPG, and shale. The analysis accommodates the influence of melting temperature, K_{GT} , and surface layer thickness, ϵ , on the pore size distribution (PSD). Calibration experiments permeated with the two fluids demonstrate that OMCTS has a larger K_{GT} and that the PSD for different cryoporometric materials is not subject to different surface curvatures of pores. Furthermore, the PSDs for shale are characterized by MICP, NAM, and NMR-C, which give comparable results. Shale samples have heterogeneous pore distributions with peak pore diameters at ~ 3 nm and mesopore diameters of 2–50 nm comprising the main storage volume. Because of its larger molecular size and correspondingly large K_{GT} , NMR-C-OMCTS is able to characterize pores to $2 \mu\text{m}$ but misses pores smaller than 5 nm. Meanwhile, NMR-C using OMCTS images a broader PSD than that by NMR-C-Water due to the propensity of OMCTS to imbibe into the organic matter relative to that of water. NMR-C-OMCTS shows the superiority and potential due to the higher signal/noise (S/N) ratio and wider measurement range up to $2 \mu\text{m}$. With regard to shales, one insight is that 115 K nm is an appropriate K_{GT} value for measurements with the surface layer thickness of 2 nm. Moreover, the applications of NMR-C-OMCTS will come down to other rocks through further research.

1. INTRODUCTION

Porous rocks that are structurally and chemically heterogeneous have important uses¹ as reservoirs for water and hydrocarbons and as barriers to flow. Transport and storage properties of such media are controlled by the pore size distribution (PSD) as this influences strength, compressibility, permeability, and development of the fracture plane.^{2,3}

Compared to conventional reservoir rocks, pores in shales vary in size from micrometers to angstroms and typically have low porosities (5–10%) and permeabilities (nano-Darcy to micro-Darcy).⁴ Pore characterization techniques applied to shales demonstrate that the pore size distribution is sensitive to both the measurement technique and experimental conditions.⁵ Some measurements are applied directly on the pores whereas others effectively measure pore throat diameters. Mercury injection capillary pressure (MICP) and the nitrogen adsorption method (NAM) measurements are commonly applied for PSD characterization for gas shales. These methods are invasive and involve intrusion of a fluid by either high-pressure mercury (MICP) or low-pressure nitrogen (NAM).⁶ Noninvasive imaging is possible through small angle neutron scattering (SANS), neutron diffraction cryoporometry (NDC), differential scanning calorimetry (DSC), and nuclear magnetic resonance (NMR), which are also able to determine PSDs.

However, most of these methods have limitations in covering a broad distribution of pore sizes from micropores to macropores with high precision.^{7,8} To cover an extended range of PSDs, different techniques are frequently used in combination. For example, NMR and small-angle X-ray scattering may be combined to characterize the pore system and flow characteristics⁹ as may be NMR and micro-CT scanning to define pore network models,¹⁰ and MICP and scanning electron microscopy¹¹ may be combined for petrophysical characterization of shale.

NMR cryoporometry (NMR-C) has been used in pore characterization of various micro- and mesoporous materials.¹² This technique involves freezing a liquid in the liquid-saturated pores and measuring the volume of liquid as the sample is incrementally warmed until all of the liquid is melted. Because the melting point is depressed for pores/crystals of small size, this melting point depression gives a measurement of pore sizes. Because NMR distinguishes between solid and liquid, quantifying only liquid mass, NMR cryoporometry obtains clear transitions with a high signal-to-noise ratio. Compared to other

Received: March 27, 2017

Revised: June 9, 2017

Published: June 21, 2017

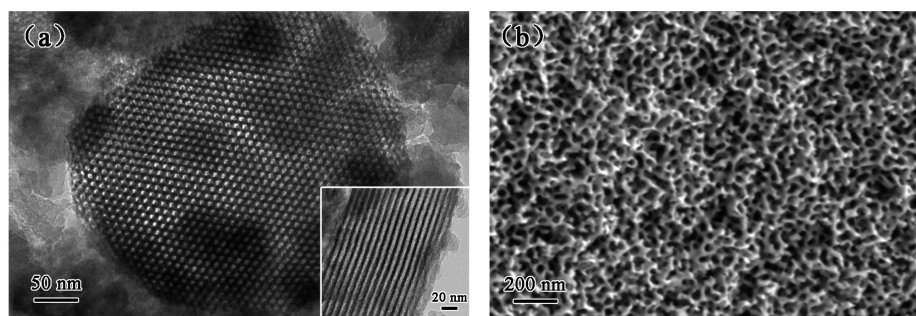


Figure 1. TEM image of (a) SBA and (b) SEM image of CPG¹² used for this study.

existing techniques, the major advantage of NMR-C is the ability to perform spatial imaging of samples in a natural hydrated state.¹³

The NMR-C method relies on a pore size-dependent melting temperature depression of a pore-filling material given by the Gibbs–Thomson equation¹⁴

$$\Delta T_m(x) = T_m^\infty - T_m(x) = \frac{4\sigma_{sl}T_m}{x\Delta H_f\rho_s} \quad (1)$$

where T_m^∞ and $T_m(x)$ are the bulk and pore melting temperatures, σ_{sl} is the solid–liquid surface free energy, ΔH_f is the latent heat of melting, ρ_s is the density of the solid, and x is the pore diameter. For arbitrarily shaped pores, $T_m(x)$ depends on the average curvature of the pore wall rather than on a uniform size parameter such as x . We may rewrite eq 1 as

$$\Delta T_m = \frac{K_{GT}}{x} \quad (2)$$

where K_{GT} is the melting point depression constant. In a typical experimental protocol, the NMR signal intensity $I(T)$ from the molten fraction of the pore-filling material is measured as the initially frozen sample is incrementally warmed. For this signal to be separated from that of the frozen fraction, a difference between transverse relaxation times T_2 in the respective states is exploited. The PSD is then calculated by numerical differentiation of $I(T)$. If the NMR signal intensity is properly calibrated in terms of the mass of the sample, the PSD can be estimated.

In NMR-C, the melting point depression constant K_{GT} defines, in combination with instrumental parameters such as temperature spread in the sample and temperature step size, the achievable resolution and the detectable upper pore size.¹⁵ Hence, choosing a probe material with a greater K_{GT} is preferable. Computing the probe material constant K_{GT} from thermodynamic properties requires knowledge of the solid–liquid surface tension, which is typically difficult to measure and is rarely available from independent experiments. Instead, K_{GT} is often calibrated from the temperature shifts for phase transitions observed in some well-defined porous materials with different pore sizes.

Water is the predominant liquid used in NMR-C measurements, which is easily imbibed into hydrophilic pores and has a low melting point depression constant. There has been a wide range of NMR-C-Water relying on the properties of water/ice systems in a confined geometry. NMR-C-Water has been widely used to image cement, wood, fuel cells, and rocks.^{16–18} In low iron and paramagnetic content materials, NMR-C-Water works well using 2τ echo sampling times of 2 ms or greater.¹⁹ If the metallic and paramagnetic contents are high, the measure-

ments should be taken at intervals of 500 μ s or less, essentially probing the brittle–plastic phase transition rather than the brittle–liquid phase transition. This yields spuriously low pore-size magnitudes and degrades accuracy. In addition, the expansion of water when freezing may damage porous media and influence the results of pore size distribution.^{19,20} Thus, further investigation focused on the suitability of polar liquids to NMR-C measurements.²¹ Cyclohexane has a long and successful history as an NMR-C probe liquid with a greater K_{GT} . Cyclohexane is an organic compound, comprising a ring molecule with a 6-fold symmetrical structure. The spin–spin relaxation time, T_2 , of liquid for cyclohexane is easily distinguishable from that of solid, the liquid T_2 is of the order of milliseconds to seconds and the solid T_2 of the order of microseconds. However, this probe fluid exhibits a bulk-phase plastic state between the solid and liquid phases and the transverse relaxation time does not change sufficiently sharply. Thus, it is well-known that measurements need to be performed with a 2τ echo time of ~ 20 ms.

Recently, octamethylcyclotetrasiloxane (OMCTS) has been observed to have a larger melting point depression constant than cyclohexane, potentially allowing access to pores >1 μ m in diameter.¹⁵ OMCTS also has the advantage of a short T_2 (~ 20 μ s) and a sharp phase transition, thus providing a clear discrimination between liquid and solid 1 H NMR signals. Additionally, OMCTS is chemically inert, nonvolatile, and nontoxic with a bulk melting point near 290 K^{22,23} and appears capable of wetting both hydrophilic and hydrophobic surfaces.^{15,24} NMR-C-OMCTS could be an effective method for characterizing nanopores in shales²⁵ but there are still questions left unanswered such as the value of K_{GT} .

The following explores the characterization of pore size distributions for shales via NMR-C using both water and OMCTS as probe fluids. The NMR-C results are compared with data from MICP and NAM. With the calibration of OMCTS as the probe fluid, it is found that OMCTS not only improves the signal/noise (S/N) ratio but also has the potential to yield PSDs for μ m sized pores while simultaneously imbibing into both organic and inorganic components. Moreover, the effects of melting point depression constant and surface layer thickness on PSD measurements are discussed, which were rarely considered in previous studies using NMR-C.

2. EXPERIMENTAL INVESTIGATION

2.1. Sample Preparation. The response of natural shale is compared with manufactured calibration samples of known topology and morphology. Calibration samples were prepared from regular templated SBA-15 porous silica consisting of cylindrical pores ~ 7 – 9 nm and from controlled pore glass (CPG) with a nominal average pore size of 24 nm (shown in Figure 1). According to TEM/SEM

Table 1. Mineral Components of the Shale Sample Measured by SEM-EDS

sample	quartz (%)	pyrite (%)	feldspar (%)	chlorite (%)	apatite (%)	calcite (%)	dolomite (%)	illite (%)	rutile (%)
shale	37.5	6.37	35.10	1.87	0.08	2.22	0.81	8.09	0.80

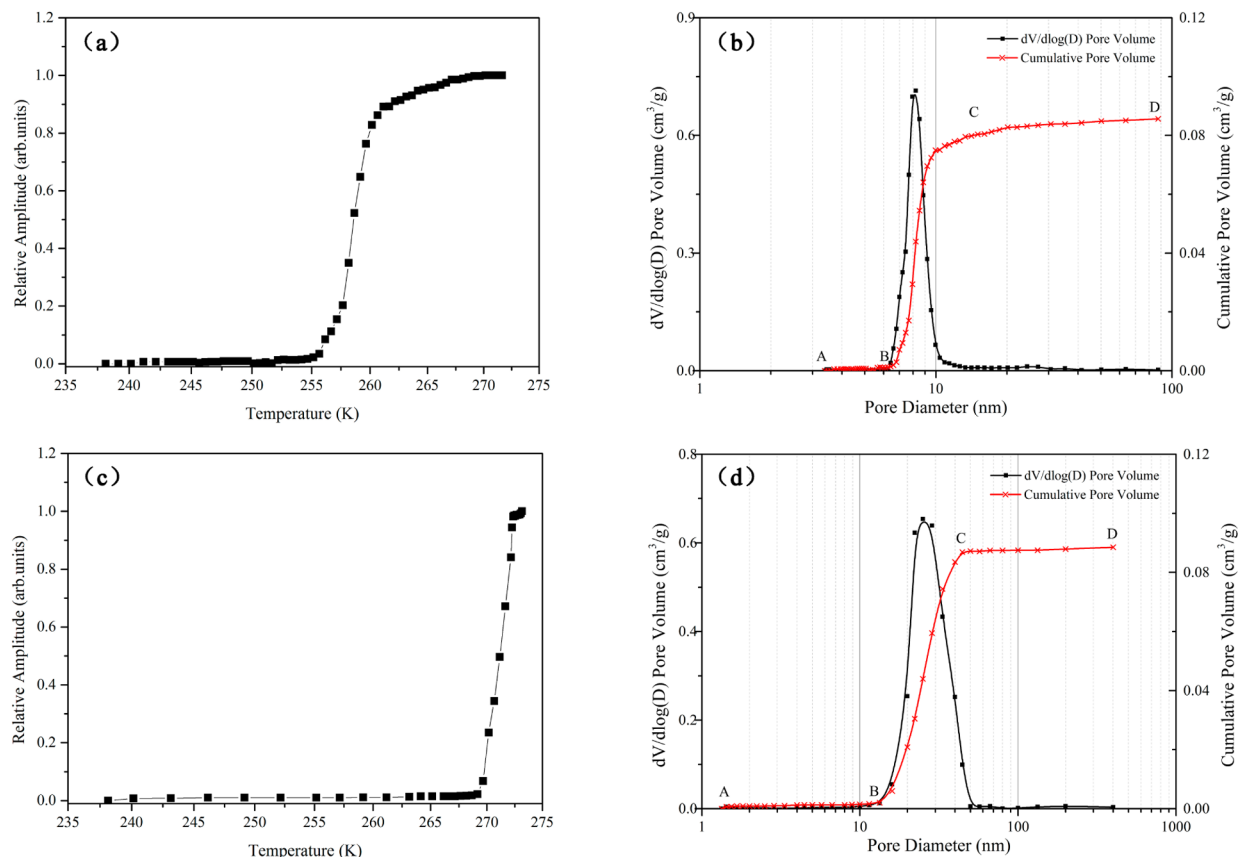


Figure 2. Data of NMR-C-Water measurements for standard samples. Echo amplitudes at 4 ms as a function of temperature for (a) SBA-15 and (c) CPG. PSDs of (b) SBA-15 (with $K_{GT} = 116 \pm 2$ K nm) and (d) CPG (with $K_{GT} = 59 \pm 1$ K nm).

images of SBA and CPG, they had average pore diameters of 8.2 nm (SBA-15) and 23.9 nm (CPG). Additionally, shale samples were collected from the Longmaxi Formation (Xiliao, Shizhu County, China) and used in comparison. The shale samples were pulverized to sizes in the range ~ 1 –2 mm for use in the NMR-C experiments with mineral compositions measured using SEM-EDS. Results are listed in Table 1. After drying at 105 °C for 24 h, the standard and shale samples were immersed in the probe liquids for ~ 10 h and then centrifuged at 5000 rpm for 3 h in 5 mm diameter thin-walled high-resolution NMR sample tubes. The tubes were 2 cm in length and capped and sealed at the top. The permeating fluids were distilled water and anhydrous OMCTS.

2.2. Experimental Protocol. The cryoporometric ^1H NMR measurements were conducted on a Niumag with a resonant frequency of 21 MHz and equipped with a 10 mm probe. The temperature control system comprises a compressor and a cooling bath with a low temperature limit of -65 °C. During the experiments, the temperature was incremented in 0.1–2 K steps and left to equilibrate for 10 min to allow for thermal equilibrium at each temperature. Temperatures are incremented in the range 240–283 K for water and 245–298 K for OMCTS (based on their bulk melting points). NMR-C measurements were performed using the Carr–Purcell–Meiboom–Gill (CPMG) pulse sequence. The spin–echo amplitude was measured with a time interval τ of 2 ms for water and 0.4 ms for OMCTS to suppress the signature of the solid and to ensure that the signal was entirely from the liquid phase. The amplitude of signal intensity at the first echo ($T = 2\tau$), representing the amount of hydrogen protons, was transformed to the volume of

liquids. Before the NMR signal intensity could be converted into pore volumes, the measured intensity was corrected by calibration using a MnCl_2 solution (concentration $\sim 0.25\%$) with T_2 of ~ 1 ms and then transformed into water mass. The OMCTS mass was measured through the ratio of unit volume signal between water and OMCTS. The cryoporometric calibration measurements were repeated at least three times for each sample. Shale samples were also characterized by MICP and NAM, and the results were then compared to measurements by scanning electron microscopy (SEM) to support pore structure interpretations. MICP measurements were performed using a Micromeritics Autopore IV 9500 instrument and run to a pressure of 0.10 psia defined as a plateau toward the maximum pressure of injection at 60000 psi. NAM measurements were completed using a 3H-2000PS2 Instrument at 77.4 K with an outgas temperature of 473 K. The experiments of NMR-C and SEM are completed in the Key Laboratory of Shale Gas and Geoenvironment of the Chinese Academy of Sciences.

3. RESULTS

3.1. Experimental Calibration of K_{GT} for Water and OMCTS. Although the melting point depression constant (K_{GT}) is a material parameter, its value usually cannot be independently estimated due to the limited accuracy of determining σ_{sl} . The K_{GT} for a given liquid must be calibrated using known pore sizes. As standard calibration samples, SBA-15 and CPG were used to calibrate the K_{GT} of both water and OMCTS in the NMR-C measurements.

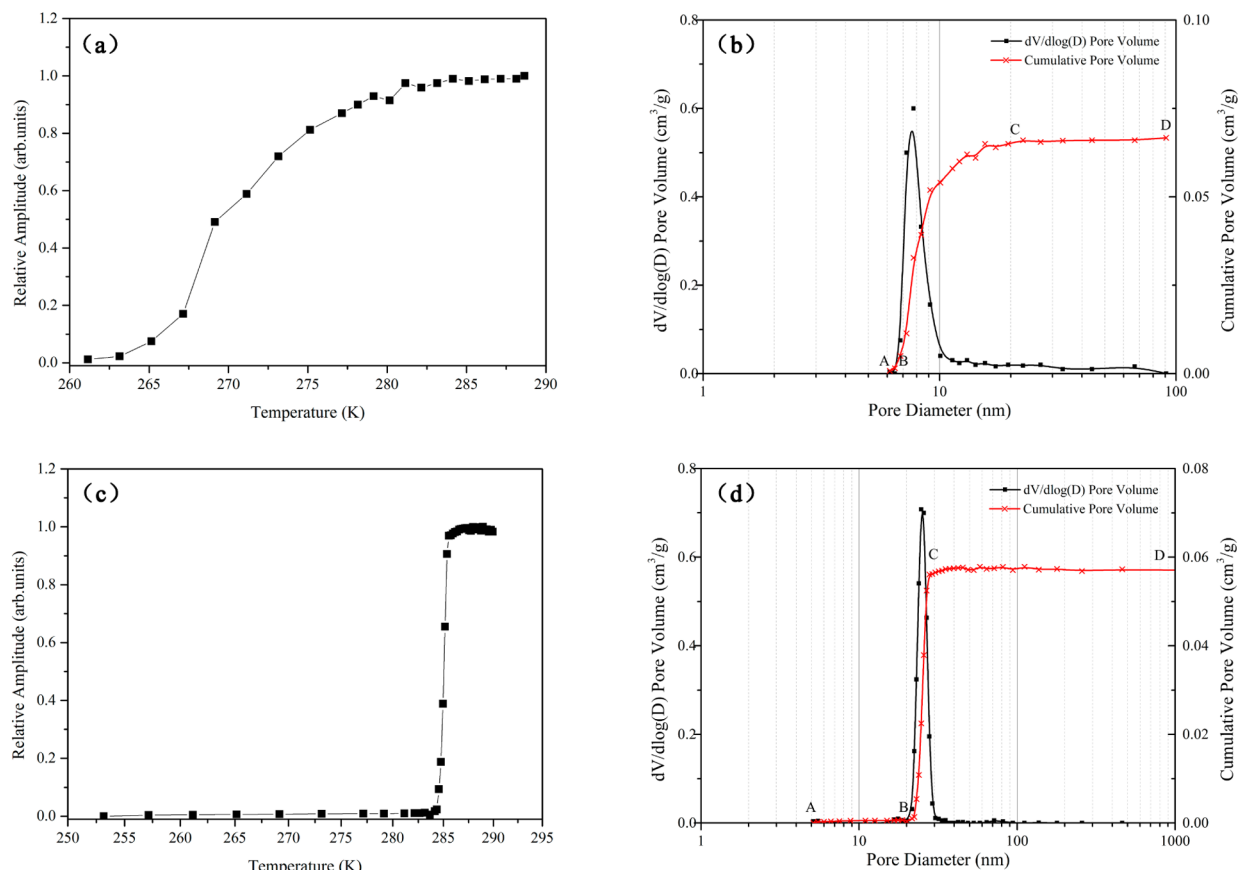


Figure 3. Data of NMR-C-OMCTS measurements for standard samples. Echo amplitudes at 0.8 ms as a function of temperature for (a) SBA-15 and (c) CPG. PSDs of (b) SBA-15 (with $K_{GT} = 122 \pm 3$ K nm) and (d) CPG (with $K_{GT} = 115 \pm 3$ K nm).

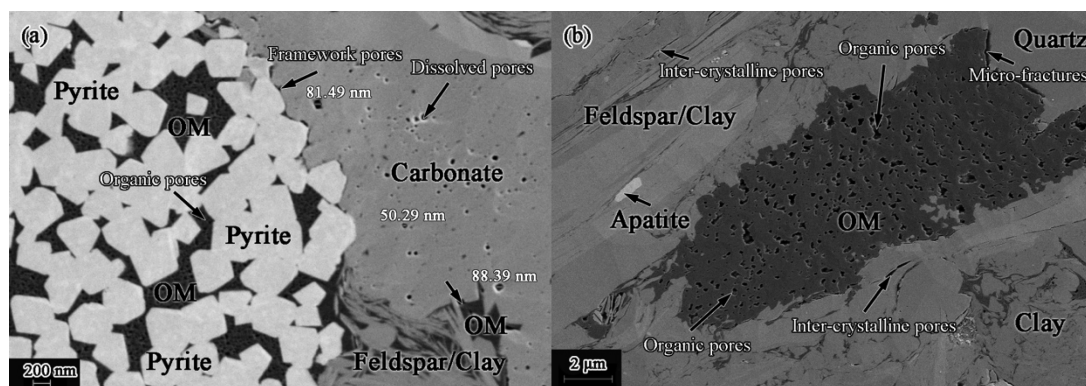


Figure 4. SEM images of contrasting pore types, including (a) organic, dissolved pores, and framework and (b) intercrystalline, microfracture, and organic.

As for NMR-C-Water, with increasing temperature for the standard samples (Figure 2(a and c)), the liquid in the pores begins to melt (Figure 2(b and d)): from B to C) with cumulative pore volume reaching a plateau when all the liquid in the pores has melted (Figure 2(b and d)): from C to D). The difference in temperature between B and C gives the melting point depression in the pores. The K_{GT} were calibrated by SBA-15 and CPG, which have an average pore diameter of 8.2 nm (SBA-15) and 23.9 nm (CPG) respectively. As a result, they obtained the best fit when $K_{GT} = 116 \pm 2$ K nm (SBA-15) and 59 ± 1 K nm (CPG) according to eq 2. The PSDs of SBA-15 and CPG from NMR-C-Water are both of the Gaussian-type NMR-C-Water, having a full width at half-maximum (fwhm) of

1.9 and 15 nm. From NMR-C-Water calibration experiments, the ratio of K_{GT} for CPG and K_{GT} for SBA is close to 1/2, which is similar to the results reported for sol-gel silicas and SBA-15.²⁶

The melting curves measured by NMR-C-OMCTS have a similar form to those for NMR-C-Water. However, when considering organic liquids such as OMCTS, the influence of the liquid-like surface layer to the signal has to be considered. Nonlinearity in the Gibbs–Thomson equation has been observed in previous work with the modified Gibbs–Thomson equation proposed as

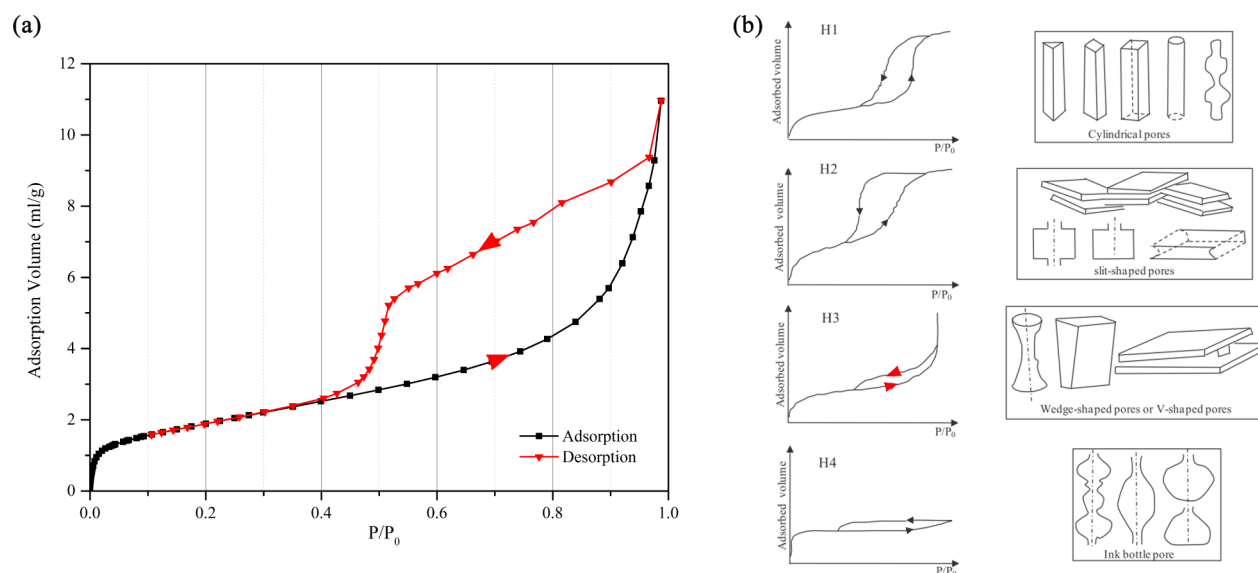


Figure 5. (a) Adsorption and desorption isotherms of NAM. (b) Types of hysteresis loops as defined by IUPAC with the corresponding pore shapes.³³

$$\Delta T_m = \frac{K_{GT}}{x - 2\varepsilon} \quad (3)$$

where ε is the width of the liquid-like layer. At a particular temperature, the thickness, ε , of the layer minimizes the interfacial interaction. Some studies have concluded that the surface layer can be approximated as two monolayers thick,^{27–29} and this assumption simplifies the problem to one of defining a single parameter. For OMCTS, with a monolayer width of 0.7–1.1 nm,³⁰ $\varepsilon = 2$ nm is adopted in this work. The K_{GT} calibrated by SBA-15 is 122 ± 3 K nm with a fwhm of 1.8 nm. As for CPG, the K_{GT} is 115 ± 3 K nm with a fwhm of 4 nm (see Figure 3). Comparing the PSDs of SBA and CPG using NMR-C-Water, the data detected by NMR-C-OMCTS have the more similar data to the results calculated by TEM/SEM images with smaller fwhms. In addition, according to eq 2, with the same gradient of temperature, the NMR-C measurements using the liquid with a larger K_{GT} , such as OMCTS, could obtain more diameter data, which means that the results measured by NMR-C-OMCTS have a significantly higher S/N than that of NMR-C-Water.

3.2. Comparison of PSDs of Shales Measured by Different Techniques. Shales have unique pore structures as a result of their complex evolution³¹ comprising multiscale pore architectures spanning nanoscale to macroscale. Longmaxi shale comprises clay minerals, quartz, feldspar, calcite, dolomite, and pyrite.³² With these complex compositional components, the pore structure of Longmaxi shale comprises multiple pore types, including organic, intercrystalline, framework, dissolution, biological pores, and microfractures. Typical SEM images are shown in Figure 4 with various minerals and pores labeled.

In this study, PSDs were characterized by three different techniques (MICP, NAM, and NMR-C). MICP is a widely accepted technique for characterizing pore throat diameters in a porous medium by recording the volume of mercury injected at each step of incremented fluid pressure. Unfortunately, MICP is incapable of quantifying the volume of the pore or the volumetric properties of those pores. The maximum injection pressure is 60000 psi (413 MPa), representing a pore throat diameter of ~ 3 nm. NAM determines the amount of gas

occupying the internal surface of a porous material and estimates the PSD for pore sizes < 100 nm. The pore size and pore volume may be estimated by the Barrett–Joyner–Halenda (BJH) model based on the adsorption curves of the isotherms. Figure 5 shows the adsorption curve and desorption hysteresis of the N_2 isotherms. Only the open pores form hysteresis loops with experimental results, suggesting that a portion of the pores are interconnected for the shales investigated here. Furthermore, different shapes of the adsorption curves represent the specific morphology of the pore system, classified as four types by IUPAC.³³ According to the characteristics of the hysteresis loops, the Longmaxi shale appears to be a combination of the integration of Type H3 shape (Figure 5). This defines wedge-shaped pores as the main type embedded in material with structural complexity, as confirmed by SEM images of shales where the type of shale pores are closer to CPG than SBA.

For the PSDs obtained by different techniques to be compared, the traces are coplotted as shown in Figure 6.

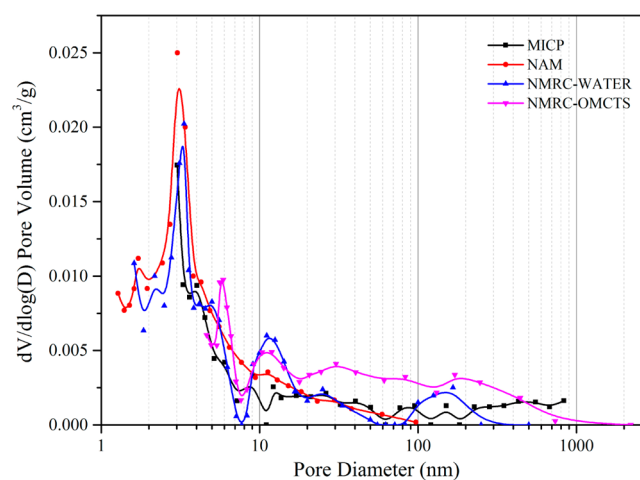


Figure 6. Comparison of pore size distributions evaluated by MICP, NAM, and NMR-C ($K_{GT} = 59$ K nm for water and $K_{GT} = 115$ K nm for OMCTS).

Shale samples have heterogeneous pore distributions with peaks at ~ 3 nm, and mesopores with diameters between 2 and 50 nm contain the major storage volume. There is good agreement across the different techniques despite the results measured by MICP usually representing a pore throat diameter. MICP and NAM are destructive techniques but are commonly used to quantify PSD for gas shales. MICP defines the average pore diameter as 17.3 nm with a porosity of 3.66%. However, the ability to probe micropores is a main limitation for MICP due to its lower threshold. Meanwhile, the surface tension and contact angle of the mercury probe fluid in shales are not well constrained.³⁴ Results from NAM are larger than the other methods defining micropore average diameters at 3.66 nm. However, the NAM analysis becomes problematic for materials with low surface area^{35,36} and with pore sizes >100 nm.

The PSDs derived from the melting behavior by NMR-C are also compared with MICP and NAM. According to the hysteresis loop obtained by NAM and the SEM images, the shale pores are closer to CPG than SBA, and the PSDs detected by NMR-C-Water (Figure 6), as calculated by $K_{GT} = 59$ K nm, are the same as the value calibrated by CPG, whereas the influence on OMCTS is less. The PSDs determined using water as the probe liquid contain details of pores below 2 nm, whereas OMCTS excludes pores below a 5 nm threshold (when $K_{GT} = 115$ K nm and $\epsilon = 2$ nm). The magnitude of the PSD obtained by OMCTS is larger than that recovered using water, especially on macropores (see Figure 7). This is also

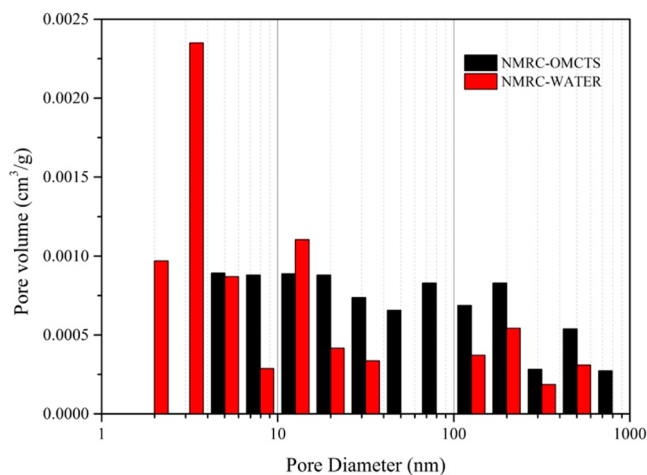


Figure 7. Comparison of bar graphs using NMR-C-Water (with $K_{GT} = 59$ K nm) and NMR-C-OMCTS (with $K_{GT} = 115$ K nm).

larger than that recovered by MICP and NAM. OMCTS is again superior to previous probe materials due to its ability to access large pores with pore sizes up to $2 \mu\text{m}$.

4. DISCUSSION

4.1. The K_{GT} of Water and OMCTS for Different Samples. The melting temperature of liquids is related to the

surface energy and depends on the geometry of the interface between the crystal and liquid. For convenience, eq 2 can be expressed in the form³⁷

$$\Delta T_m = \frac{K_{GT}}{x} = \frac{k_g k_s k_i}{x} \quad (4)$$

where k_g is a structural geometric factor depending on the interfacial shape, k_s is a constant describing the crystalline solid of the solid–liquid system, and k_i is an interfacial energy term. The term k_g/x is related to the surface-to-volume (S/V) ratio for different media. SBA-15 is a highly regular material containing cylindrical pores on a hexagonal lattice with a very narrow pore distribution.³⁸ Conversely, CPG is fabricated via spinodal decomposition with ligaments of a complex non-cylindrical geometry.^{24,39} The shape indicator value of CPG falls between cylinders and spheres due to the random and interconnected tubular shape of the pores. Thus, K_{GT} evaluated by eq 2 and modeled for cylindrical pores may provide the main difference between the different samples. It is noteworthy that the relative magnitude of K_{GT} for OMCTS for different cryoporometric materials is not subject to this limitation.¹⁵ In addition, the property of liquids may be the main factor contributing to the different behaviors of K_{GT} . The values of K_{GT} in earlier studies are summarized in Table 2. Actually, water is a liquid most strongly subject to thermodynamic fluctuations, especially coupling with porous media of disordered pore structure.⁴⁰ Because of this, the evident variation of K_{GT} occurs in different porous materials in terms of water.

Because of various pore formation mechanisms, each type of pore is distinguished by its pore size, shape, and environment. For example, organic pores are predominantly round or oval in shape and are relatively small in size, and dissolution usually occurs in carbonates and feldspars with microfractures zigzagged in shape and with high tortuosity, all of which influence the magnitude of the K_{GT} in term of surface curvature and may introduce a large error to the interpreted PSD. For shales with a broad range of structural features (size and form), OMCTS with its broad operating range will be superior compared to other cryoporometric materials. Actually, the $K_{GT} = 115$ K nm of OMCTS is a reference value for shale measurements considering the existence of surface layers, which will be discussed in section 4.2.

4.2. Effect of Surface Layer for OMCTS. Stapf and Kimmich (1995)⁴⁵ suggested that fluid-mineral surface layers may interfere with the interpretation of NMR cryoporometry by providing a signal even at very low temperatures, which can be misinterpreted as indicating the presence of very small pores. The effect of the surface layer may be diminished by lengthening the total echo time. The signal of water in pores is not highly sensitive to ϵ within the time interval, 2τ , of 4 ms. However, to some extent, the signal and the width of a surface layer may influence the results of PSDs when using OMCTS in pore diameters <40 nm (Table 3). Comprehensive analyses of the melting point depression data show that the best fit is

Table 2. Cryoporometrically Relevant Physical Properties of OMCTS (ϵ is the Thickness of the Surface Layer)

probe liquid	K_{GT} calibrated by different samples (K nm)				
	Sol–gel	SBA	MCM	CPG	
water	57.3 ¹ , 58.2 ¹⁶ 53 ⁴¹	140, ²⁶ 116.4 \pm 0.5 ³⁸	51.9, ⁴² 52 \pm 2 ⁴³	48 \pm 0.8, ¹⁵ 50 ⁴⁴	
OMCTS				113 \pm 3 ($\epsilon = 2$), ¹⁵ 160 \pm 4 ($\epsilon = 0$) ¹⁵	

Table 3. Cryoporometrically Relevant Physical Properties of OMCTS¹⁵

liquid	ΔH_f (kJ/mol)	ν (m ³ /mol)	σ_{sl} (mJ/m ²)	ζ (nm)
OMCTS	19.7	279.8×10^{-6}	14	1.45

obtained using $x - 2\epsilon$ rather than just x . Considering the assumption of ϵ approximated as two monolayers in thickness, we obtained $K_{GT} = 112 \pm 2$ K nm with $\epsilon = 2.2$ nm and $K_{GT} = 121 \pm 3$ K nm with $\epsilon = 1.4$ nm, as calibrated by CPG. If the surface layer is neglected, the estimated K_{GT} will be 135 ± 3 K nm. Vargas-Florencia et al. (2007) define $K_{GT} = 136 \pm 7$ K nm and $\epsilon = 1.1 \pm 0.3$ nm by leaving ϵ as a free variable. According to previous studies, the surface layer continuously thickens with increasing temperature while simultaneously being influenced by the surface curvature.⁴⁶ Petrov and Furó (2006) found that the maximum layer thickness of six uncoated controlled pore glasses varied from approximately 2 to 5 monolayers. They suggest a relation to estimate ϵ_{max} by assuming $\partial^2 F / \partial t^2 = 0$, where F is the free energy and t is an arbitrary layer thickness for a system. The resulting equation is

$$\epsilon_{max} \equiv \epsilon(T_m) = 1/(2\kappa) - \zeta/2 - (\sigma_{sl} T_m^\infty \nu / \Delta H_f) / (T_m^\infty - T_m) \quad (5)$$

where κ is the integral pore curvature, ζ is a correlation length of the crystalline order in the nonfreezing region, and ν is the molar volume. According to the results of MICP, S/V of the sample is 0.231/nm, and κ is 65.9×10^{-3} /nm assuming $2\kappa/(S/V) = 0.57$ (for CPG). The simplified equation yields $\epsilon_{max} = 6.86 - 57.74/(T_m^\infty - T_m)$, and yield an ϵ_{max} value of 6.86 nm, which is 1.28 nm also calculated by NAM. The results of ϵ_{max} have certain differences due to the main distinction in testing range for MICP and NAM methods.

However, the influence of ϵ decreases in the larger pores. According to the data measured by Petrov and Furó (2006),¹² the errors measured for six CPGs vary from 10.97 to 53.3% without considering the presence of surface layers (see Table 4). Conversely, the errors can be <10% when setting $\epsilon = 2$ nm.

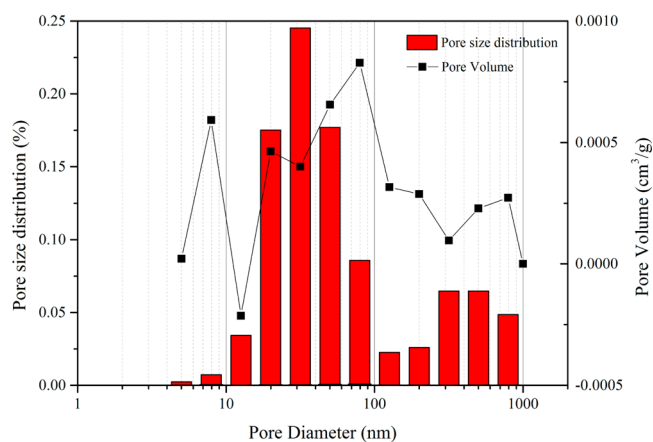
Table 4. Errors of PSDs for Six CPGs Calculated through Various Values of Surface Layers

thickness of surface layer (ϵ)	error (%)					
	CPG75	CPG115	CPG156	CPG237	CPG313	CPG729
$\epsilon = 0$	53.33	39.13	33.33	23.21	17.89	10.97
$\epsilon = 2$	0	4.35	7.69	6.32	5.11	5.50

In summary, the effect of a surface layer to probing by OMCTS is affected by temperature and surface curvature and needs to be further constrained. Meanwhile, ϵ may become a major influencing parameter to the measurement of mesopores (especially on pores <10 nm) when OMCTS is used. Nevertheless, on the basis of previous work, there is a valid modification if two monolayer layer thickness is assumed for OMCTS. This conclusion is important when measuring complex porous media with mixed pore shapes.

4.3. Wettability of Shales and Resulting PSDs by Water and OMCTS. Shale reservoirs are presumed to have originated as organic rich mud deposited in a marine environment, suggesting they were initially water wet.⁴⁷ As a complex sedimentary rock, shale is a mixture of minerals and organic matter. Different minerals and organic materials

naturally have different wetting properties. Thus, the wettability of shale is very complex due to the mixture of different wetting components.⁴⁸ The quartz, feldspar, dolomite, and clay minerals are hydrophilic, and the organic components of the rock are hydrophobic.^{49,50} The total organic carbon (TOC) contents of the Longmaxi shales range from 0.35 to 18.4% with an average of 2.52%, indicating that the Longmaxi shales are rich in organic matter. As demonstrated in Figure 4, organic matter can be embedded between brittle and clay minerals. The size of organic pores range from several to hundreds of nanometers. The mineral composition of this sample is listed in Table 1 with the organic matter comprising 6.8% (analyzed by Avizo). The PSD of the organic pores was estimated from SEM images with the results shown in Figure 8. These results may be

**Figure 8.** (a) PSD of organic pores calculated from SEM images (bars). (b) Volume difference for pores measured by water and by OMCTS as measured from Figure 7 (points).

used to explain the pore volume difference recovered by NMR-C-Water and NMR-C-OMCTS. Although SEM only observes the internal surface of a shale specimen and is frequently used for qualitative analysis, it does provide a direct and intuitive method for characterizing pore features. The prevailing organic pores range in size from 20 to 100 nm, and the possible ability of OMCTS to imbibe onto both organic and inorganic matrices may explain the stronger intensity from it for water because water can only imbibe into hydrophilic pores. Because shale has both hydrophilic and hydrophobic pore surfaces inside both organic and mineral components, OMCTS is a superior probe fluid because it seems to intrude into both hydrophobic and hydrophilic surfaces. NMR-C-OMCTS will reflect true pore volume, which most useful in evaluating gas storage and transport characteristics.

5. CONCLUSIONS

PSDs of shale play a significant role in gas storage and transport in shales. Compared to other porosimetric techniques such as gas and mercury porosimetry, NMR-C has the advantage of enabling examination of the samples in a hydrated state, which means that choosing an appropriate probe liquid has great significance.

In NMR-C, the melting point depression constant K_{GT} defines the achievable resolution and detectable upper pore size. Calibration experiments permeated with the two fluids demonstrate that the measured ratio $K_{GT} = 59 \pm 1$ K nm (CPG)/ $K_{GT} = 116 \pm 2$ K nm (SBA) for water is $\sim 1/2$, whereas

$K_{GT} = 115 \pm 3 \text{ K nm}$ (CPG) and $K_{GT} = 122 \pm 3 \text{ K nm}$ (SBA) for OMCTS is ~ 1 . It is noteworthy that OMCTS has a larger K_{GT} and that the PSD for different cryoporometric materials is not subject to different surface curvatures of pores. Meanwhile, the transverse relaxation time of OMCTS differs by more than 3 orders of magnitude between the solid and liquid states with high signal/noise (S/N) ratio, especially on pores $>10 \text{ nm}$. Upon comparing six CPGs, surface layer ε may become a major influencing parameter for the measurement of mesopores for OMCTS, and errors of PSD can be $<10\%$ when setting $\varepsilon = 2 \text{ nm}$ (roughly two monolayers thick). Furthermore, the PSDs for shales are characterized by MICP, NAM, and NMR-C, which give comparable results. Shale samples have heterogeneous pore distributions with peak pores at $\sim 3 \text{ nm}$ and mesopore diameters of $2\text{--}50 \text{ nm}$ comprising the main storage volume. Because of its larger molecular size and correspondingly large K_{GT} , NMR-C-OMCTS is able to characterize pores to $2 \mu\text{m}$ but misses pores smaller than 5 nm . Meanwhile, $K_{GT} = 115 \text{ K nm}$ for OMCTS is an appropriate value for shale measurements with the surface layer thickness of 2 nm . In addition, NMR-C-OMCTS images a broader PSD than that by NMR-C-water ($20\text{--}100 \text{ nm}$) due to the propensity of OMCTS imbibing into the organic matter relative to water.

In other words, OMCTS is a potential probe liquid with a melting point depression larger than that of others, which seems to intrude into both hydrophilic and hydrophobic pore surfaces. This work compares results of PSDs using NMR-C-Water and NMR-C-OMCTS in term of the melting temperature of liquids and surface layers, further giving the reference values of parameters used in shale measurements. Actually, the method of NMR-C-OMCTS may have many applications outside of shales, such as for granite and limestone, due to its scale of pore size up to the micrometer range and wetting properties. However, the effect of uncertain surface layers plays a remarkable role in micropores and mesopores, which requires further work if using OMCTS as a probe liquid for NMR-C.

AUTHOR INFORMATION

Corresponding Author

*E-mail: dongyh@mail.iggcas.ac.cn.

ORCID

Yanhui Dong: 0000-0003-4815-8600

Notes

The authors declare no competing financial interest.

ACKNOWLEDGMENTS

The research was financially supported by the Strategic Priority Research Program of the Chinese Academy of Sciences (Grant XDB10030601). Partial support was also provided by the Youth Innovation Promotion Association CAS (Grant 2016063) and the China Scholarship Council (Grant 201504910044). We are grateful to the anonymous reviewers for their constructive comments and suggestions that greatly improved the manuscript.

ABBREVIATIONS

PSD, pore size distribution; MICP, mercury injection capillary pressure; NAM, nitrogen adsorption method; SANS, small-angle neutron scattering; NDC, neutron diffraction cryoporometry; DSC, differential scanning calorimetry; NMR, nuclear magnetic resonance; NMR-C, nuclear magnetic resonance cryoporometry; K_{GT} , melting point depression constant;

OMCTS, octamethylcyclotetrasiloxane; CPMG, Carr–Purcell–Meiboom–Gill; CPG, controlled pore glass; SEM, scanning electron microscopy; fwhm, full width at half-maximum; BJH, Barrett–Joyner–Halenda; TOC, total organic carbon

REFERENCES

- (1) Webber, J. B. W. *Characterising porous media*; University of Kent at Canterbury: Canterbury, UK, 2000.
- (2) Kate, J. M.; Gokhale, C. S. A simple method to estimate complete pore size distribution of rocks. *Eng. Geol.* **2006**, *84* (1–2), 48–69.
- (3) Song, Y. Q.; Ryu, S.; Sen, P. N. Determining multiple length scales in rocks. *Nature* **2000**, *406* (6792), 178–81.
- (4) Bertonecello, A.; Honarpour, M. M. Standards for characterization of rock properties in unconventional reservoirs: fluid flow mechanism, quality control, and uncertainties. SPE Annual Technical Conference and Exhibition. Society of Petroleum Engineers, 2013.
- (5) Hinai, A. A.; Rezaee, R.; Esteban, L.; et al. Comparisons of pore size distribution: A case from the Western Australian gas shale formations. *Journal of Unconventional Oil and Gas Resources* **2014**, *8*, 1–13.
- (6) Clarkson, C. R.; Solano, N.; Bustin, R. M.; et al. Pore structure characterization of North American shale gas reservoirs using USANS/SANS, gas adsorption, and mercury intrusion. *Fuel* **2013**, *103* (1), 606–616.
- (7) Clarkson, C. R.; Freeman, M.; He, L.; et al. Characterization of tight gas reservoir pore structure using USANS/SANS and gas adsorption analysis. *Fuel* **2012**, *95*, 371–385.
- (8) Labus, M.; Labus, K.; Bujok, P. *Eage Shale Workshop* **2016**, 1.
- (9) Bustin, R. M.; Bustin, A. M. M.; Cui, A., et al. Impact of Shale Properties on Pore Structure and Storage Characteristics. Society of Petroleum Engineers, 2008.
- (10) Talabi, O.; Alsayari, S.; Iglauer, S.; et al. Pore-scale simulation of NMR response. *J. Pet. Sci. Eng.* **2009**, *67* (3–4), 168–178.
- (11) Kale, S.; Rai, C.; Sondergeld, C. Rock typing in gas shales. SPE Annual Technical Conference and Exhibition. Society of Petroleum Engineers, 2010.
- (12) Petrov, O.; Furó, I. Curvature-dependent metastability of the solid phase and the freezing-melting hysteresis in pores. *Phys. Rev. E* **2006**, *73* (1), 302–309.
- (13) Kraemer, S. V.; Sagidullin, A. I.; Lindbergh, G.; et al. Pore Size Distribution and Water Uptake in Hydrocarbon and Perfluorinated Proton-Exchange Membranes as Studied by NMR Cryoporometry. *Fuel Cells* **2008**, *8* (3–4), 262–269.
- (14) Jackson, C. L.; Mckenna, G. B. The melting behavior of organic materials confined in porous solids. *J. Chem. Phys.* **1990**, *93* (12), 9002–9011.
- (15) Vargas-Florencia, D.; Petrov, O. V.; Furó, I. NMR Cryoporometry with octamethylcyclotetrasiloxane as a probe liquid. Accessing large pores. *J. Colloid Interface Sci.* **2007**, *305* (2), 280–285.
- (16) Mitchell, J.; Webber, J. B. W.; Strange, J. H. Nuclear magnetic resonance Cryoporometry. *Phys. Rep.* **2008**, *461* (1), 1–36.
- (17) Jeon, J. D.; Kwak, S. Y. Ionic cluster size distributions of swollen nafion/sulfated β -cyclodextrin membranes characterized by nuclear magnetic resonance Cryoporometry. *J. Phys. Chem. B* **2007**, *111* (32), 9437–9443.
- (18) Zhao, Y.; Sun, Y.; Liu, S.; et al. Pore structure characterization of coal by NMR Cryoporometry. *Fuel* **2017**, *190*, 359–369.
- (19) Matsumoto, M. Why does water expand when it cools? *Phys. Rev. Lett.* **2009**, *103* (1), 017801.
- (20) Takarli, M.; Prince, W.; Siddique, R. Damage in granite under heating/cooling cycles and water freeze–thaw condition. *INT. J. ROCK MECH. MIN.* **2008**, *45* (7), 1164–1175.
- (21) Webber, J. B. W.; Strange, J. H.; Bland, P. A., et al. Dynamics at Surfaces: Probing the Dynamics of Polar and A-Polar Liquids at Silica and Vapour Surfaces. Hürlimann, M. D., Song, Y. Q., Fantazzini, P., Eds.; AIP Conference Proceedings. AIP, 2008; Vol. 1081, Issue 1, pp 51–54.

- (22) Luu, H. M.; Hutter, J. C. Bioavailability of octamethylcyclotetrasiloxane (D(4)) after exposure to silicones by inhalation and implantation. *Environ. Health Perspect.* **2001**, *109* (11), 1095–1101.
- (23) Tavana, H.; Simon, F.; Grundke, K.; et al. Interpretation of contact angle measurements on two different fluoropolymers for the determination of solid surface tension. *J. Colloid Interface Sci.* **2005**, *291* (2), 497–506.
- (24) Petrov, O. V.; Dulce Vargaflorencia, A.; Furó, I. Surface Melting of Octamethylcyclotetrasiloxane Confined in Controlled Pore Glasses: Curvature Effects Observed by ¹H NMR. *J. Phys. Chem. B* **2007**, *111* (7), 1574–81.
- (25) Zhou, B.; Han, Q.; Yang, P. Characterization of Nanoporous Systems in Gas Shales by Low Field NMR Cryoporometry. *Energy Fuels* **2016**, *30* (11), 9122–9131.
- (26) Webber, J. B. W. Studies of nano-structured liquids in confined geometries and at surfaces. *Prog. Nucl. Magn. Reson. Spectrosc.* **2010**, *56* (1), 78–93.
- (27) Schreiber, A.; Ketelsen, I.; Findenegg, G. H. Melting and freezing of water in ordered mesoporous silica materials. *Phys. Chem. Chem. Phys.* **2001**, *3* (7), 1185–1195.
- (28) Gedat, E.; Schreiber, A.; Albrecht, J.; et al. H-2-solid-state NMR study of benzene-d(6) confined in mesoporous silica SBA-15. *J. Phys. Chem. B* **2002**, *106* (8), 1977–1984.
- (29) Aksnes, D. W.; Førland, K.; Stöcker, M. ¹H NMR relaxation and diffusion studies of cyclohexane and cyclopentane confined in MCM-41. *Microporous Mesoporous Mater.* **2005**, *77* (1), 79–87.
- (30) Horn, R. G.; Israelachvili, J. N. Direct measurement of structural forces between two surfaces in a nonpolar liquid. *J. Chem. Phys.* **1981**, *75* (3), 1400–1411.
- (31) Bustin, R. M.; Bustin, A. M. M.; Cui, A.; et al. Impact of shale properties on pore structure and storage characteristics. SPE shale gas production conference. Society of Petroleum Engineers, 2008.
- (32) Zhang, Q.; Liu, R.; Pang, Z.; et al. Characterization of microscopic pore structures in Lower Silurian black shale(S 1 I), southeastern Chongqing, China. *Mar. Pet. Geol.* **2016**, *71*, 250–259.
- (33) Sing, K. S. W. Reporting physisorption data for gas/solid systems with special reference to the determination of surface area and porosity (Recommendations 1984). *Pure Appl. Chem.* **1985**, *57* (4), 603–619.
- (34) Wang, S.; Javadpour, F.; Feng, Q. Confinement Correction to Mercury Intrusion Capillary Pressure of Shale Nanopores. *Sci. Rep.* **2016**, *6*, 20160.
- (35) Suzuki, I.; Oosawa, K. Measurement of 0.1 cm² surface areas by xenon adsorption at liquid oxygen temperature using an adsorption apparatus with a temperature-compensated, differential tensimeter of symmetrical design. *Rev. Sci. Instrum.* **1997**, *68* (12), 4531–4535.
- (36) Yanazawa, H.; Ohshika, K.; Matsuzawa, T. Precision Evaluation in Kr Adsorption for Small BET Surface Area Measurements of Less Than 1 m². *Adsorption* **2000**, *6* (1), 73–77.
- (37) Webber, J. B. W.; Dore, J. C.; Strange, J. H.; et al. Plastic ice in confined geometry: the evidence from neutron diffraction and NMR relaxation. *J. Phys.: Condens. Matter* **2007**, *19* (41), 3385–3391.
- (38) Webber, J. B. W.; Dore, J. C. Neutron Diffraction Cryoporometry—A measurement technique for studying mesoporous materials and the phases of contained liquids and their crystalline forms. *Nucl. Instrum. Methods Phys. Res., Sect. A* **2008**, *586* (2), 356–366.
- (39) Kucheyev, S. O.; Van Cleve, E.; Worsley, M. A. Freezing and melting of hydrogen confined in nanoporous silica. *J. Phys.: Condens. Matter* **2014**, *26* (22), 225004–225004.
- (40) Kondrashova, D.; Valiullin, R. Freezing and melting transitions under mesoscale confinement: Application of the Kossel–Stranski crystal-growth model. *J. Phys. Chem. C* **2015**, *119* (8), 4312–4323.
- (41) Morishige, K.; Kawano, K. Freezing and melting of water in a single cylindrical pore: The pore-size dependence of freezing and melting behavior. *J. Chem. Phys.* **1999**, *110* (10), 4867–4872.
- (42) Jähnert, S.; Vaca, C. F.; Schaumann, G. E.; et al. Melting and freezing of water in cylindrical silica nanopores. *Phys. Chem. Chem. Phys.* **2008**, *10* (39), 6039–6051.
- (43) Schreiber, A.; Ketelsen, I.; Findenegg, G. H. Melting and freezing of water in ordered mesoporous silica materials. *Phys. Chem. Chem. Phys.* **2001**, *3* (7), 1185–1195.
- (44) Petrov, O. V.; Furó, I. A joint use of melting and freezing data in NMR Cryoporometry. *Microporous Mesoporous Mater.* **2010**, *136* (1–3), 83–91.
- (45) Stapf, S.; Kimmich, R.; Seitter, R. Proton and deuteron field-cycling NMR relaxometry of liquids in porous glasses: Evidence for Levy-walk statistics. *Phys. Rev. Lett.* **1995**, *75* (15), 2855–2858.
- (46) Engemann, S. Premelting at the ice–SiO₂ interface: a high-energy x-ray microbeam diffraction study. 2005. *Uni Stuttgart - Universitätsbibliothek*, **2005**.
- (47) Passey, Q. R.; Bohacs, K.; Esch, W. L., et al. From oil-prone source rock to gas-producing shale reservoir-geologic and petrophysical characterization of unconventional shale gas reservoirs. International oil and gas conference and exhibition in China. Society of Petroleum Engineers, 2010.
- (48) Mehana, M.; Elmonier, I. Shale characteristics impact on Nuclear Magnetic Resonance (NMR) fluid typing methods and correlations. *Pet.* **2016**, *2* (2), 138–147.
- (49) Mitchell, A. G.; Hazell, L. B.; Webb, K. J. Wettability determination: pore surface analysis. SPE Annual Technical Conference and Exhibition. Society of Petroleum Engineers, 1990.
- (50) Dehghanpour, H.; Lan, Q.; Saeed, Y.; et al. Spontaneous imbibition of brine and oil in gas shales: effect of water adsorption and resulting microfractures. *Energy Fuels* **2013**, *27* (6), 3039–3049.